


# Superconducting nanowire single photon detector with efficiency over 90% at 2 μm wavelength

Zhen Wan(万震), Jia Huang(黄佳), Guangzhao Xu(徐光照), Yu Ding(丁钰), Xiaoyu Liu(刘晓宇), Yiming Pan(潘一铭), Hongxin Xu(徐鸿鑫), Hao Li(李浩), and Lixing You(尤立星)

**Citation:**Chin. Phys. B, 2026, 35 (**1**): 018501. DOI: 10.1088/1674-1056/ae1b79
http://cpb.iphy.ac.cn; http://iopscience.iop.org/cpb

**What follows is a list of articles you may be interested in**

---

## Single-flux-quantum-based qubit control with tunable driving strength

Kuang Liu(刘匡), Yifan Wang(王一凡), Bo Ji(季波), Wanpeng Gao(高万鹏), Zhirong Lin(林志荣), and Zhen Wang(王镇)

Chin. Phys. B, 2023, 32 (**12**): 128501. DOI: 10.1088/1674-1056/acf5d0

## Implementation of an 8-bit bit-slice AES *S*-box with rapid single flux quantum circuits

Ruo-Ting Yang(杨若婷), Xin-Yi Xue(薛新伊), Shu-Cheng Yang(杨树澄), Xiao-Ping Gao(高小平), Jie Ren(任洁), Wei Yan(严伟), and Zhen Wang(王镇)

Chin. Phys. B, 2022, 31 (**9**): 098501. DOI: 10.1088/1674-1056/ac70b9

## Characterization of topological phase of superlattices in superconducting circuits

Jianfei Chen(陈健菲), Chaohua Wu(吴超华), Jingtao Fan(樊景涛), and Gang Chen(陈刚)

Chin. Phys. B, 2022, 31 (**8**): 088501. DOI: 10.1088/1674-1056/ac5612

## Photodetectors based on junctions of two-dimensional transition metal dichalcogenides

Xia Wei(魏侠), Fa-Guang Yan(闫法光), Chao Shen(申超), Quan-Shan Lv(吕全山), Kai-You Wang(王开友)

Chin. Phys. B, 2017, 26 (**3**): 038504. DOI: 10.1088/1674-1056/26/3/038504

## High efficiency, large-active-area superconducting nanowire single-photon detectors

Gu Min (顾敏), Zhang La-Bao (张蜡宝), Kang Lin (康琳), Zhao Qing-Yuan (赵清源), Jia Tao (郏涛), Wan Chao (万超), Xu Rui-Ying (徐睿莹), Yang Xiao-Zhong (杨小忠), Wu Pei-Heng (吴培亨), Zhang Yong (张永), Xia Jin-Song (夏金松)

Chin. Phys. B, 2015, 24 (**6**): 068501. DOI: 10.1088/1674-1056/24/6/068501

---

**RAPID COMMUNICATION**

# Superconducting nanowire single photon detector with efficiency over 90% at 2 μm wavelength

Zhen Wan(万震)[1,2,3,†], Jia Huang(黄佳)[2,†,‡], Guangzhao Xu(徐光照)[4,†,§], Yu Ding(丁钰)[4], Xiaoyu Liu(刘晓宇)[2], Yiming Pan(潘一铭)[5], Hongxin Xu(徐鸿鑫)[2], Hao Li(李浩)[1,2,¶], and Lixing You(尤立星)[2]

[1] *Shanghai Research Center for Quantum Sciences, Shanghai* 201315, *China*
[2] *National Key Laboratory of Materials for Integrated Circuits, Shanghai Institute of Microsystem and Information Technology, Chinese Academy of Sciences (CAS), Shanghai* 200050, *China*
[3] *School of Microelectronics, Shanghai University, Shanghai* 201800, *China*
[4] *Photon Technology (Zhejiang) Co., Ltd., Zhejiang* 314100, *China*
[5] *School of Information Science and Engineering, NingboTech University, Ningbo* 315100, *China*

(Received 2 September 2025; revised manuscript received 29 October 2025; accepted manuscript online 5 November 2025)

We here report a high system detection efficiency (SDE) superconducting single-photon detector (SSPD) at 2 μm wavelength. The device integrates a $SiO_2/Ta_2O_5$ distributed Bragg reflector (DBR) and a sandwich-structured double-layer NbN nanowire to enhance the optical absorption efficiency. A cold development technique is implemented to optimize the superconducting nanowires with sub-40-nm linewidths, thus enhancing the intrinsic detection efficiency (IDE). The fabricated SSPD shows an SDE exceeding 90% at 2 μm wavelength. Moreover, the detector allows an operational working temperature of 2.2 K provided by a compact GM cryo-cooler. This detector delivers excellent performance at the 2 μm wavelength, and its optimized structural design implies promising potential for extending detection toward longer infrared bands. It thus holds value for advancing high-sensitivity quantum technologies, mid-infrared optical communications, and dark matter detection research.

**Keywords:** superconducting single-photon detectors (SSPDs), system detection efficiency, near infrared

**PACS:** 85.25.–j, 42.60.Lh, 95.85.Jq

**DOI:** 10.1088/1674-1056/ae1b79 **CSTR:** 32038.14.CPB.ae1b79

## 1. Introduction

As a high-performance single-photon detection technology, superconducting single-photon detectors (SSPDs) have demonstrated irreplaceable application value in cutting-edge fields such as quantum information,[1,2] deep space optical communications,[3] and biological fluorescence detection.[4] Compared with traditional semiconductor detection devices like single-photon avalanche diodes (SPADs)[5] and photomultiplier tubes (PMTs),[6] SSPDs exhibit significant advantages in terms of system detection efficiency (SDE),[7–9] dark count rate (DCR),[10] timing jitter ($T_j$),[11] and counting rate (CR).[12] Currently, SSPDs have achieved high SDE in the visible to near-infrared (NIR) wavelength range. Particularly in the 1550 nm band, which is widely used in optical communication and quantum communication, they have realized nearly 100% detection efficiency.[7–9]

Meanwhile, SSPDs have demonstrated significant performance potential in the mid-infrared (MIR) band. This is particularly evident in key fields: free-space optical communication,[13] where MIR atmospheric transmission windows facilitate improved long-distance signal transmission; environmental monitoring,[14] enabling precise detection of trace gases via their characteristic MIR absorption; and biomedical applications,[15] supporting label-free molecular sensing through faint MIR emissions from biological tissues.

Typically, our SDE is calculated as $\mathrm{SDE} = \eta_{\mathrm{cou}} \times \eta_{\mathrm{abs}} \times \eta_{\mathrm{det}}$, where $\eta_{\mathrm{cou}}$ represents the coupling efficiency, $\eta_{\mathrm{abs}}$ denotes the absorption efficiency, and $\eta_{\mathrm{det}}$ stands for the intrinsic detection efficiency (IDE). In recent years, many research teams have reported achieving saturated quantum efficiency in the mid-infrared band, meaning they have realized 100% IDE.[16–20] However, translating this theoretical performance into practical MIR SSPDs with high detection efficiency still requires overcoming numerous technical challenges. The primary challenge is to enhance the optical absorption efficiency in the MIR band, which serves as the core prerequisite for achieving high SDE. Another critical issue is the need to precisely control the linewidth uniformity and edge quality of

[†] These authors contributed equally to this work.
[‡] Corresponding author. E-mail: huangj@mail.sim.ac.cn
[§] Corresponding author. E-mail: gzxu@cnphotec.com
[¶] Corresponding author. E-mail: lihao@mail.sim.ac.cn

© 2026 Chinese Physical Society and IOP Publishing Ltd. All rights, including for text and data mining, AI training, and similar technologies, are reserved.

nanowires while ensuring a practical photosensitive area size, thereby avoiding IDE loss caused by fabrication defects. Overcoming these challenges is crucial for MIR SSPDs to advance from laboratory-level performance to practical applications.

At present, the development of MIR SSPDs with high detection efficiency still faces numerous challenges. Meanwhile, the development maturity of optical components and supporting instruments corresponding to the MIR band is far lower than that of the NIR band. Therefore, many research teams have prioritized their research focus on achieving high-efficiency detection of SSPDs operating at the 2 μm band. As a transitional region between the NIR and MIR bands, the 2 μm band serves as a key detection window in multiple basic scientific research fields. On one hand, this band is highly matched with the characteristic vibrational energy levels of greenhouse gases such as methane and carbon dioxide; thus, SSPDs with high detection efficiency can enable high-sensitivity spectral analysis of these molecules, providing more accurate technical support for environmental science research including Earth meteorology.[21] On the other hand, in the fields of remote sensing and security,[22] detectors working at the 2 μm band can penetrate complex environments such as light fog and smoke, and are applicable to practical scenarios including low-altitude UAV remote sensing and infrared early warning for border security. Recently, several research teams have made notable progress in the 2 μm wavelength band.[23–25] Among them, Delft university achieved an SDE of over 70% by fabricating nanowires using NbTiN.[24] Building on NbTiN nanowires, the NICT team designed a new structure of dielectric multilayer cavities (DMC), achieving an SDE of 84.1%.[25]

Here, we report a SSPD with a SDE exceeding 90% at the 2 μm wavelength band. This outcome marks a pioneering achievement, as high-efficiency detection at this specific band using a double-layer superconducting nanowire configuration has not been realized in prior studies. To reach this high-performance milestone in the target band, we integrated a sandwich-structured (double-layer) superconducting nanowire with a distributed Bragg reflector (DBR) mirror. This tailored combination maximizes light trapping within the active region, effectively addressing the inherent challenge of low absorption for 2 μm NIR photons. Meanwhile, we optimized device fabrication by adopting a cold development process, which significantly reduces the roughness of superconducting nanowires and directly boosts the detector's IDE. Notably, this detector can operate stably at 2.2 K, a temperature far higher than the ultra-low cryogenic conditions required by most comparable 2 μm SSPDs, greatly enhancing its practicality and operational convenience. This work not only delivers a high-performance 2 μm SSPD but also provides a novel, replicable technical route, offering important support for advancing the application of SSPDs in the long-wavelength near-infrared band.

## 2. Device design and fabrication

To enable SSPDs to operate at longer wavelengths while maintaining excellent performance, it is necessary to satisfy both extreme optical absorption and high IDE.[26] Therefore, we have made corresponding designs for both aspects. First, regarding optical absorption, we optimized the device structure by drawing inspiration from Hu's design.[8] A superconducting nanowire with a thickness of 6/3/6 nm was fabricated using a NbN/$SiO_2$/NbN sandwich structure on a DBR structure. This optical structure features a DBR mirror composed of 15 alternating layers of $SiO_2$ and $Ta_2O_5$, deposited on the backside of a silicon substrate that has been thermally oxidized on both sides. Additionally, a double-layer superconducting nanowire structure made of two NbN films was employed, separated by an $SiO_2$ insulator to enhance photon absorption. We simulated this optical structure using the finite element software COMSOL Multiphysics. As shown in Fig. 1(a), the reflectivity at 2 μm is 99.6%, while the optical absorption rate of the nanowire is 98.5%. This lays a foundation for us to develop SSPD with higher SDE.

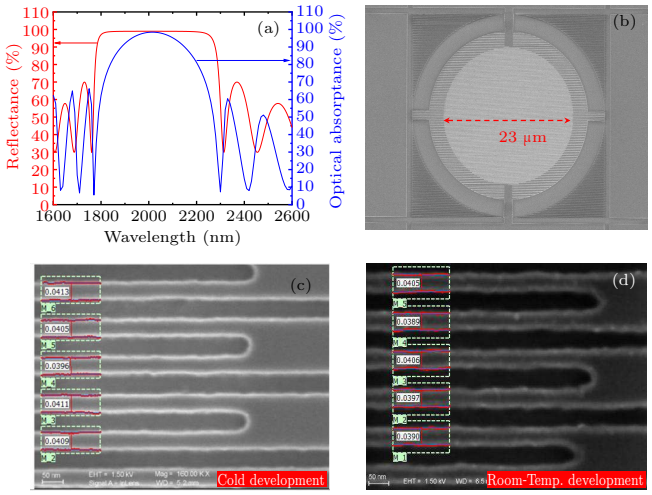



**Fig. 1.** (a) The reflection of photons across different wavelength bands by the DBR optical structure (red line) and the corresponding optical absorption of nanowires (blue line) were simulated using COMSOL software. In the simulation, the thickness of the layer $Ta_2O_5$ is 240 nm, the layer $SiO_2$ is 345 nm, and the layer NbN is 6 nm. The corresponding refractive indices are $n_{Ta_2O_5} = 2.076$, $n_{SiO_2} = 1.448$, $n_{NbN} = 4.98 + 4.49i$. (b) SEM image of the active region of the SSPD, illustrating that the active region has a diameter of 23 μm. (c) Magnified view of the local nanowires under cold development conditions. (d) Magnified view of the local nanowires under room-temperature development conditions.

A straightforward and effective strategy to improve the IDE is reducing the width of nanowires to enhance the photon sensitivity.[27] To this end, we introduced a cold development process that simultaneously achieves narrow linewidths and reduced line-edge roughness (LER). As the dissolution rate of the exposed resist decreases at lower temperatures, patterning resolution is improved.

The specific fabrication process of the device is as follows. First, 15 layers of periodic $SiO_2/Ta_2O_5$ quarter-wave stacks (with a center wavelength of 2 μm) were deposited on a 2-inch silicon substrate using ion-beam-assisted deposition. During the deposition process, the thickness of the optical films is monitored in real-time to ensure it matches the design value. Next, the bottom and top NbN films, each 6 nm thick, were deposited at room temperature in an $Ar/N_2$ gas environment using direct current magnetron sputtering. In the middle, a 3 nm thick $SiO_2$ insulating layer was deposited by plasma-enhanced chemical vapor deposition (PECVD). Double-layer nanowires were fabricated in a single etching step via electron-beam lithography (EBL) and reactive ion etching (RIE). The diluted positive-tone ZEP520 resist was spin-coated at 3500 rpm for 45 s and prebaked at 180 °C for 5 min, yielding a resist thickness of 90 nm. The samples were exposed using an EBL system at a 100 kV acceleration voltage with a beam current of 100 pA. Cold development demonstrated superior resolution, enhanced resist contrast, and reduced LER compared to room-temperature processes by selectively dissolving low-molecular-weight polymer fragments while suppressing the dissolution of high-MW chains through kinetic energy reduction and elevated glass transition temperatures.[28,29] Post-exposure processing involved 30 s of development in n-amyl acetate and 60 s of isopropanol rinse at $\sim 0$ °C. Nanowire transfer was accomplished via $CF_4$ plasma etching, with final electrode microbridges patterned by ultraviolet lithography.

Figure 1(b) shows a scanning electron microscopy (SEM) image of the device's active region, which features a circular area 23 μm in diameter. A close-up view of the nanowires with parabolic corners designed to alleviate critical current crowding is provided in Fig. 1(c). The linewidth and LER were characterized using top-view SEM imaging.[30] By applying an image-based edge detection algorithm, the nanowire edges were identified, and deviations from an ideal smooth contour were statistically analyzed across five uniformly spaced locations along multiple nanowires. This analysis yielded an average linewidth of about 40 nm with a pitch of 90 nm, and an LER value of 1.9 nm, expressed as three times the standard deviation ($3\sigma$) of the edge position fluctuations. It should be noted that the data presented in Figs. 1(c) and 1(d) are only partial results; the final LER value was calculated using ProSEM, the software equipped with the SEM, based on a larger set of measurement data. As shown in Fig. 1(d), under room-temperature (Room-Temp.) development conditions, nanowires with comparable linewidths ($\approx 40$ nm) exhibit an LER of 3.9 nm. In contrast, our cold development process enables a certain improvement in LER performance, with the value reduced to 1.9 nm, which confirms the efficacy of our proposed method.

## 3. Measurements and results

To package the device, we need to align the fiber with the active region to ensure that the fiber's focused spot accurately illuminates the center of the active region. In this process, we use a single-mode fiber (Thorlabs-SM1950), which has excellent transmission performance for photons in the wavelength range from visible light to 2200 nm and a spot size (7 μm) smaller than that of the active region. An anti-reflection coating (ARC), optimized for the study's key wavelength band, was deposited on the single-mode fiber's end face to reduce fiber-air interface Fresnel reflection loss. After completing the optical alignment, the device is installed on a secondary cryostat based on a GM cooling system. Since single-mode fibers (SMFs) exhibit high bending loss sensitivity at the 2000 nm wavelength, which suppresses the transmission of long-wavelength photons, it is crucial to minimize fiber bending during installation.[31]

Figure 2(a) shows the experimental optical path and circuit built to characterize the performance of the device. First, 2000 nm laser pulses are generated by a thulium-doped fiber laser (Thorlabs-LFL2000). The laser pulses are transmitted through SMF connected to four attenuators, which include two fixed attenuators at 1550 nm (EXFO-FVA-3150), one custom 2000 nm fixed attenuator (QOPTRONIC-LQ-VOA-2000), and finally one variable 2000 nm attenuator (EXFO-FTB-3500-B-EI). The fiber then connects to a squeeze-type polarization controller (Thorlabs-PLC900) to control the polarization of the light, and the light is finally fed into our SSPD. The bias current is provided to the device through the DC port of a Bias-T by a DC voltage source in series with a 100 kΩ resistor. The voltage pulses generated by the SSPD are transmitted to the RF port of the biasing system and amplified using a room-temperature 50 dB low-noise amplifier (RF Bay Inc.-LNA650). The amplified pulse signals are counted by a photon counter and analyzed by a computer for data processing.

The experimental setup for power calibration is also illustrated in Fig. 2(a). During the calibration process, we employed an optical power meter (Thorlabs-PM100D) equipped with an integrating sphere photodiode power sensor (Thorlabs-S148C) to determine the actual optical power at a 2000 nm wavelength. For single-photon detection applications with a target photon flux of $10^6$ photons/s, the corresponding required optical power is $-100.027$ dBm. However, our tests revealed that when the power meter is set to the 2000 nm band, its readings become unreliable below $-30$ dBm. To address this limitation, we implemented a four-attenuator configuration to ensure all calibration measurements remain above $-30$ dBm.

The calibration protocol consists of three main steps. First, we individually calibrated three fixed attenuators to achieve 30 dB of attenuation each, using the power meter to

verify the attenuation before resetting them to zero. Second, we connected the power meter at the output of the polarization controller and adjusted the fourth, tunable attenuator to obtain a reading of −10.027 dBm. Finally, we engaged all attenuators to their target attenuation values, completing the full optical path power calibration.

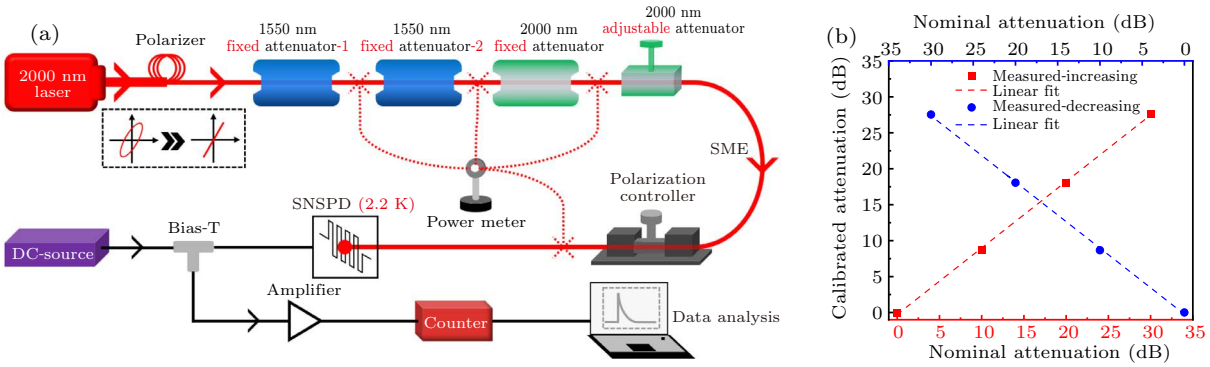



**Fig. 2.** (a) System schematic for characterizing SSPD. Photons generated by the laser propagate through the fiber, sequentially pass through a polarizer, three fixed attenuators, one variable attenuator, and one squeezed-type polarization controller, finally illuminate our SSPD. The DC voltage source powers the SSPD via a Bias-T, and the electrical signal generated by the SSPD is read out through the Bias-T and an amplifier into a counter, with data analysis performed on a computer. (SMF: single-mode fiber). (b) Linearity test of a 2000 nm custom attenuator. The red and blue curves represent fitting results for the attenuator's increasing and decreasing linearity, respectively. The fitted increasing slope is 0.979, and the decreasing slope is 0.980.

We conducted a linearity test on the attenuation variation of the custom attenuators. As shown in Fig. 2(b), the fitted slopes for the increasing and decreasing paths are 0.979 and 0.980, respectively, both very close to the ideal value of 1. This indicates a high linear relationship between the actual attenuation values and the nominal attenuation values of the attenuators. The slope being slightly less than 1 suggests a slight deviation in the actual attenuation values, but the deviation is minimal and within acceptable error limits. The slope for the decreasing path is almost identical to that of the increasing path, indicating excellent response consistency in both the increasing and decreasing directions of the attenuator, with no significant hysteresis.

Figure 3 shows the relationship between SDE and DCR as functions of bias current for the device operating in the 2 μm wavelength band. Through testing, the switching current of this device was 5.3 μA. When the bias current was 4.7 μA, the SDE reached 91.09%, with a DCR of 4.4 kHz. We also fitted the SDE curve and calculated that our IDE is approximately 99.78% based on the fitted data. If we want to further improve this, we can place the device in a lower-temperature system for operation. Since no measures were taken to suppress dark counts in this system, the DCR was relatively high, primarily due to blackbody radiation and stray light entering through the fused fiber from the room-temperature environment. In practical applications, various filtering techniques can be employed to reduce the DCR, such as placing a bandpass filter (BPF)[32] at 4 K temperature, integrating a BPF on the substrate,[33] or integrating a BPF on the end face of the coupling fiber.[34] Additionally, due to fluctuations in measuring tools and the measurement process, there were some deviation in the results. The relative uncertainty of the SDE ($\sigma_{\mathrm{SDE}}$) was determined by all possible uncertainties in the measurements as follows:[35]

$$\sigma_{\mathrm{SDE}} = \sqrt{\sigma_{\mathrm{m}}^2 + \sigma_{\mathrm{r}}^2 + \sigma_{\mathrm{tr}}^2}, \tag{1}$$

$$\sigma_{\mathrm{m}} = \sqrt{\sigma_{\mathrm{pm}}^2 + \sigma_{\mathrm{l}}^2 + \sigma_{\lambda}^2}, \tag{2}$$

$$\sigma_{\mathrm{r}} = \sqrt{\sigma_{\mathrm{att}}^2 + \sigma_{\mathrm{p}}^2}, \tag{3}$$

$$\sigma_{\mathrm{tr}} = \sqrt{\sigma_{\mathrm{f}}^2 + \sigma_{\mathrm{t}}^2 + \sigma_{\mathrm{c}}^2 + \sigma_{\mathrm{a}}^2}. \tag{4}$$

We have classified each uncertainty component: $\sigma_{\mathrm{m}}$ represents core measurement instruments uncertainty, $\sigma_{\mathrm{r}}$ stands for optical regulation devices uncertainty, and $\sigma_{\mathrm{tr}}$ denotes optical transmission losses uncertainty. To quantify the uncertainties in SDE measurements, each loss factor was measured at least five times, and the corresponding uncertainties were estimated accordingly. The specific definition of each uncertainty component is illustrated in the notes of Table 1. By combining these uncertainty values with Eqs. (1)–(4) and the data in Table 1, the uncertainty of the SDE was calculated to be 6.09%, which is also marked as a red shaded area in the SDE curve of Fig. 3 for clarity.

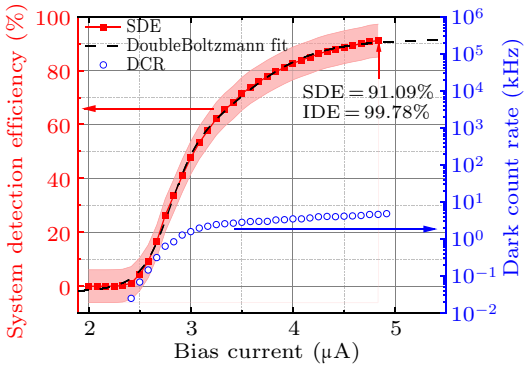



**Fig. 3.** SDE and DCR of the SSPD in the 2 μm wavelength band as functions of bias current.

**Table 1.** Possible uncertainties in SDE measurements.

| Factor | Relative uncertainty (%) |
|---|---|
| $\sigma_{pm}$ | 5.00 |
| $\sigma_{l}$ | 0.80 |
| $\sigma_{\lambda}$ | 0.02 |
| $\sigma_{att}$ | 3.30 |
| $\sigma_{p}$ | 0.19 |
| $\sigma_{f}$ | 0.56 |
| $\sigma_{t}$ | 0.30 |
| $\sigma_{c}$ | 0.10 |
| $\sigma_{a}$ | 0.50 |
| $\sigma_{SDE}$ | 6.09 |

$\sigma_{pm}$: The uncertainty of the optical power meter.
$\sigma_{l}$: The uncertainty of the laser source.
$\sigma_{\lambda}$: The wavelength uncertainty of the laser source.
$\sigma_{att}$: The combined uncertainty of the four attenuators.
$\sigma_{p}$: The uncertainty of the optical power fluctuation caused by the polarization controller.
$\sigma_{f}$: The uncertainty of the fiber splicing loss.
$\sigma_{t}$: The uncertainty of the optical transmission loss.
$\sigma_{c}$: The uncertainty of the coupling loss.
$\sigma_{a}$: The uncertainty of the absorption due to polarization.

We measured the timing jitter $T_j$ of the SSPD system using time-correlated single photon counting (TCSPC).[36] The synchronization signal from the light source is sent to the "Start" port of a commercial TCSPC module (Becker-Hickl, SPC-150) via a frequency converter. The amplified voltage signal of the single-photon response is then sent to the "Stop" port of the SPC-150. For SSPDs, this distribution typically appears as a Gaussian curve, from which the system timing jitter can be obtained, defined as the full width at half maximum (FWHM) of the time-correlated photon counting histogram. The measured data is shown in Fig. 4, with a $T_j$ of approximately 165 ps. The black curve in the figure represents a Gaussian fit of the data, and the fitted Gaussian peak highly overlaps with the measured data curve, indicating that the model effectively captures the main distribution characteristics of the $T_j$.

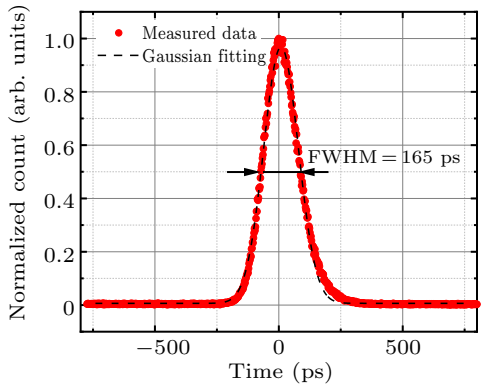



**Fig. 4.** Time-correlated photon counting histogram (red) and Gaussian fit of the data (black) measured at a wavelength of 2 μm and a bias current of 4.7 μA. The measured timing jitter ($T_j$) is 165 ps.

Dead time is defined as the time width at $1/e$ of the maximum pulse amplitude, during which the device cannot perform photon detection, reflecting the detection speed of the device. To test the speed of our device, we captured a pulse waveform response using an oscilloscope at a bias current of 4.7 μA, as shown in Fig. 5(a), and measured the dead time to be 127 ns. Figure 5(b) illustrates the trend of SDE versus input photon rates. Due to the dead time, as the input photon rate increases, the SDE decreases continuously. It can be observed that when the input photon rate reaches 37 MHz, our SDE decreases to 45.5%. Notably, when the SDE drops to half of its maximum value, the maximum count rate (MCR) is 16.8 MHz. The detection speed is primarily constrained by the nanowire length and the recovery time of the readout circuit. Since our active area is designed to be relatively large and the nanowires are narrow, the length of the nanowires becomes relatively long. The longer the nanowires, the greater the dynamic inductance they introduce, which significantly limits the detection speed of our device. To further improve the detection speed in the future, optimizations can be made to the dynamic inductance of the SSPD or to the readout circuit using techniques such as direct current coupling[37] or resistor networks.[38]

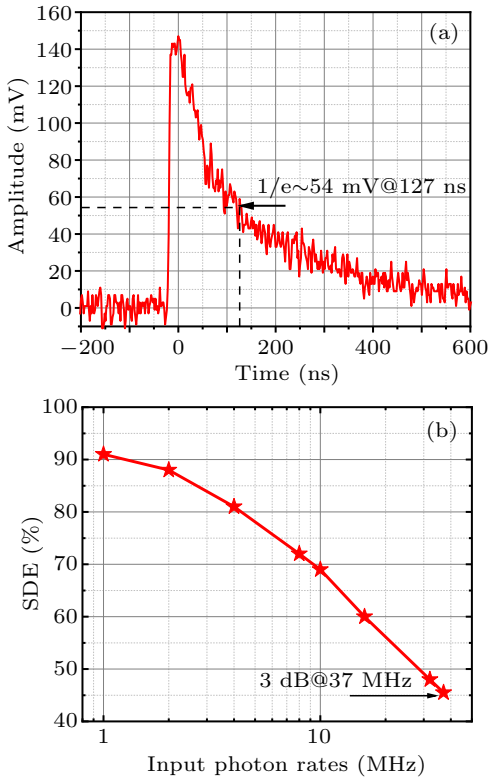



**Fig. 5.** (a) Oscilloscope response at a bias current of 4.7 μA shows a dead time of 127 ns, measured at the 1/e pulse amplitude. (b) The trend of SDE with respect to input photon rates indicates that when the input photon rate reaches 37 MHz, the SDE decreases to 45.5%. Notably, when the SDE drops to half of its maximum value, the corresponding MCR is 16.8 MHz.

As shown in Table 2, we present a comparison of the performance parameters of our work with those of other reported SSPD works in the 2 μm band, including operating temperature, process, SDE, DCR, $T_j$, and MCR. It should be noted

that the core focus of our research and design work is to optimize the detection efficiency of the detector. Therefore, among the aforementioned performance indicators, SDE is the most prominent advantage of our proposed SSPD. Specifically, our work achieves an SDE of 91.09% at an operating temperature of 2.2 K, which is notably higher than the values in Ref. [18] (63% at 2.25 K), 19 (70% at 2.5–2.8 K), and 20 (84.1% at 0.76 K). This clear superiority in SDE, compared with previously published research results, fully demonstrates the effectiveness of our design strategy centered on detection efficiency optimization.

That said, our work still has room for improvement in overall performance compared with Ref. [19]. Reference [19] exhibits lower DCR and $T_j$, highlighting the aspects we need to enhance. For reducing DCR, as mentioned earlier in this manuscript, we plan to adopt fiber end-face filtering or on-chip filtering techniques in future studies to suppress DCR. For optimizing $T_j$, two feasible approaches are under consideration: one is to improve the device structure by reducing the nanowire length, which can mitigate the impact of inductance on $T_j$; the other is to use a low-temperature amplifier, which is also an effective way to further optimize $T_j$ performance. By implementing these targeted optimization strategies in subsequent work, we aim to further balance high SDE with low DCR and $T_j$, ultimately developing a 2 μm-band SSPD with more competitive performance.

**Table 2.** Comparison of different SSPD works.

| Ref. | Temperature (K) | Process | SDE (%) | DCR (kHz) | $T_j$ (ps) | MCR (MHz) |
|---|---|---|---|---|---|---|
| [18] | 2.25 | Room-Temp. development | 63 | 12 | 102 | 12 |
| [19] | 2.5–2.8 | Room-Temp. development | 70 | 0.1 | 14.3 | / |
| [20] | 0.76 | Room-Temp. development | 84.1 | 24.4 | / | / |
| **Our work** | **2.2** | **Cold development** | **91.09** | **4.4** | **165** | **16.8** |

## 4. Conclusions

In summary, this study proposes a sandwiched double-layer NbN SSPD based on a DBR ($SiO_2/Ta_2O_5$) structure, utilizing cold development lithography techniques to fabricate ultra-narrow nanowires, thereby effectively enhancing the detector's detection efficiency. Notably, this work represents a pioneering advance in achieving high-efficiency detection in the 2 μm wavelength band through a double-layer nanowire structure. Our work focuses on characterizing and optimizing the detector's performance exclusively in the 2 μm wavelength band. The active area of the SSPD demonstrated in this paper has a diameter of 23 μm and operates at 2.2 K. When the photon flux reaches $10^6$ photons/s, the SDE exceeds 90% at this specific wavelength. This high SDE not only verifies the outstanding performance of the proposed SSPD but also confirms the feasibility of its structural design.

For future research directions, we plan to further optimize the thickness of the dielectric layers in the $SiO_2/Ta_2O_5$ DBR and adjust the superconductivity parameters of the NbN nanowires, with the goal of extending the detector's operating range to longer wavelength bands and systematically testing its performance there. Overall, the results of this work lay a solid foundation for the development of high-efficiency SSPDs, offering promising application prospects particularly in fields such as high-sensitivity quantum detection, optical communication, and infrared applications.

## Acknowledgements

This work was supported by the Strategic Priority Research Program of Chinese Academy of Sciences (Grant No. XDA0520403), Shanghai Municipal Science and Technology Major Project (Grant No. 2019SHZDZX01)), Innovation Program for Quantum Science and Technology (Grant No. 2023ZD0300100), and the National Natural Science Foundation of China (Grant Nos. U24A20320 and 62401554).

## Data availability statement

The data that support the findings of this study are openly available in Science Data Bank at https://doi.org/10.57760/sciencedb.j00113.00269.

## References

[1] Maring N, Fyrillas A, Pont M, *et al.* 2024 *Nat. Photon.* **18** 603
[2] Du F F, Fan G, Wu Y M and Ren B C 2023 *Chin. Phys. B* **32** 060304
[3] Wollman E E, Allmaras J P, Beyer A D, Korzh B, Runyan M C, Narváez L, Farr W H, Marsili F, Briggs R M, Miles G J and Shaw M D 2024 *Opt. Express* **32** 48185
[4] Wang F, Ren F, Ma Z, Qu L, Gourgues R, Xu C, Baghdasaryan A, Li J, Zadeh I E, Los J W N, Fognini A, Qin-Dregely J and Dai H 2022 *Nat. Nanotechnol.* **17** 653
[5] Bi Y H, Bian D J, Li M and Xu Y 2025 *Chin. Phys. B* **34** 068501
[6] Sadygov Z, Sadigov A and Khorev S 2020 *Phys. Part. Nuclei Lett.* **17** 160
[7] Chang J, Los J W N, Tenorio-Pearl J O, Noordzij N, Gourgues R, Guardiani A, Zichi J R, Pereira S F, Urbach H P, Zwiller V, Dorenbos S N and Esmaeil Zadeh I 2021 *APL Photonics* **6** 036114
[8] Hu P, Li H, You L, Wang H, Xiao Y, Huang J, Yang X, Zhang W, Wang Z and Xie X 2020 *Opt. Express* **28** 36884

[9] Reddy D V, Nerem R R, Nam S W, Mirin R P and Verma V B 2020 *Optica* **7** 1649
[10] Chiles J, Charaev I, Lasenby R, Baryakhtar M, Huang J, Roshko A, Burton G, Colangelo M, Van Tilburg K, Arvanitaki A, Nam S W and Berggren K K 2022 *Phys. Rev. Lett.* **128** 231802
[11] Korzh B, Zhao Q Y, Allmaras J P, *et al.* 2020 *Nat. Photonics* **14** 250
[12] Zhang T, Huang J, Zhang X, Ding C, Yu H, Xiao Y, Lv C, Liu X, Wang Z, You L, Xie X and Li H 2024 *Photon. Res.* **12** 1328
[13] Bellei F, Cartwright A P, McCaughan A N, Dane A E, Najafi F, Zhao Q and Berggren K K 2016 *Opt. Express* **24** 3248
[14] Larsson J, Bood J, Xu C T, Yang X, Lindberg R, Laurell F and Brydegaard M 2019 *Opt. Express* **27** 17348
[15] Song G, Qin T, Liu H, Xu G B, Pan Y Y, Xiong F X, Gu K S, Sun G P and Chen Z D 2010 *Lung Cancer* **67** 227
[16] Taylor G G, MacKenzie E N, Korzh B, Morozov D V, Bumble B, Beyer A D, Allmaras J P, Shaw M D and Hadfield R H 2022 *Appl. Phys. Lett.* **121** 214001
[17] Pan Y, Zhou H, Zhang X, Yu H, Zhang L, Si M, Li H, You L and Wang Z 2022 *Opt. Express* **30** 40044
[18] Chang J, Los J W N, Gourgues R, Steinhauer S, Dorenbos S N, Pereira S F, Urbach H P, Zwiller V and Esmaeil Zadeh I 2022 *Photon. Res.* **10** 1063
[19] Verma V B, Korzh B, Walter A B, Lita A E, Briggs R M, Colangelo M, Zhai Y, Wollman E E, Beyer A D, Allmaras J P, Vora H, Zhu D, Schmidt E, Kozorezov A G, Berggren K K, Mirin R P, Nam S W and Shaw M D 2021 *APL Photonics* **6** 056101
[20] Chen Q, Ge R, Zhang L, Li F, Zhang B, Jin F, Han H, Dai Y, He G, Fei Y, Wang X, Wang H, Jia X, Zhao Q, Tu X, Kang L, Chen J and Wu P 2021 *Science Bulletin* **66** 965
[21] Wang J, Liu C, Min M, Hu X, Lu Q and Husi L 2018 *IEEE Trans. Geosci. Remote Sensing* **56** 5207
[22] Taylor G G, Morozov D, Gemmell N R, Erotokritou K, Miki S, Terai H and Hadfield R H 2019 *Opt. Express* **27** 38147
[23] Zhou H, Pan Y, You L, Li H, Wang Y, Tang Y, Wang H, Liu X and Wang Z 2019 *IEEE Photonics J.* **11** 1
[24] Chang J, Los J W N, Gourgues R, Steinhauer S, Dorenbos S N, Pereira S F, Urbach H P, Zwiller V and Esmaeil Zadeh I 2022 *Photon. Res.* **10** 1063
[25] China F, Yabuno M, Mima S, Miyajima S, Terai H and Miki S 2023 *Opt. Express* **31** 20471
[26] Xu G Z, Zhang W J, You L X, Xiong J M, Sun X Q, Huang H, Ou X, Pan Y M, Lv C L, Li H, Wang Z and Xie X M 2021 *Photon. Res.* **9** 958
[27] Marsili F, Bellei F, Najafi F, Dane A E, Dauler E A, Molnar R J and Berggren K K 2012 *Nano Lett.* **12** 4799
[28] Ocola L E and Stein A 2006 *J. Vac. Sci. Technol. B* **24** 3061
[29] Tobing L Y M, Tjahjana L and Zhang D H 2012 *J. Vac. Sci. Technol. B* **30** 051601
[30] Xu G, Zhang W, You L, Wang Y, Xiong J, Fan D H, Wu L, Yu H, Li H and Wang Z 2023 *Opt. Express* **31** 16348
[31] Marcuse D 1993 *IEEE J. Quantum Electron.* **29** 2957
[32] Shibata H, Shimizu K, Takesue H and Tokura Y 2013 *Appl. Phys. Express* **6** 072801
[33] Yang X, Li H, Zhang W, You L, Zhang L, Liu X, Wang Z, Peng W, Xie X and Jiang M 2014 *Opt. Express* **22** 16267
[34] Zhang W J, Yang X Y, Li H, You L X, Lv C L, Zhang L, Zhang C J, Liu X Y, Wang Z and Xie X M 2018 *Supercond. Sci. Technol.* **31** 035012
[35] Marsili F, Verma V B, Stern J A, Harrington S, Lita A E, Gerrits T, Vayshenker I, Baek B, Shaw M D, Mirin R P and Nam S W 2013 *Nat. Photon.* **7** 210
[36] You L, Yang X, He Y, Zhang W, Liu D, Zhang W, Zhang L, Zhang L, Liu X, Chen S, Wang Z and Xie X 2013 *AIP Advances* **3** 072135
[37] Kerman A J, Rosenberg D, Molnar R J and Dauler E A 2013 *J. Appl. Phys.* **113** 144511
[38] Zhao Q, Jia T, Gu M, Wan C, Zhang L, Xu W, Kang L, Chen J and Wu P 2014 *Opt. Lett.* **39** 1869